



Zinc oxides by thermal decomposition synthesis and parameters affecting electrocatalyst activity for CO₂ reduction reaction

Elías Rodríguez-Jara^{a,b}, Margherita Cavallo^c, Ryosuke Nakazato^d, Matthias Quintelier^e, Keeko Matsumoto^d, Joke Hadermann^e, Jadra Mosa^a, Francesca Bonino^c, Kiyoharu Tadanaga^d, Mario Aparicio^a, Nataly Carolina Rosero-Navarro^{a,*}

^a Instituto de Cerámica y Vidrio (ICV), CSIC, Madrid 28049, Spain

^b Escuela de Doctorado UAM, Centro de Estudios de Posgrado, Universidad Autónoma de Madrid. C/Francisco Tomás y Valiente, nº 2. Ciudad Universitaria de Cantoblanco, 28049 Madrid, Spain

^c Department of Chemistry, NIS and INSTM Reference Centers, Università di Torino, Via Quarello 15/A, 10135 Torino, Italy

^d Faculty of Engineering, Hokkaido University, Sapporo, Hokkaido 060-8628, Japan

^e EMAT, Department of Physics, University of Antwerp, 2020 Antwerp, Belgium

ARTICLE INFO

Keywords:

ZnO
Electrocatalyst
CO₂
CO production
Thermal decomposition
Faradaic efficiency
Morphology

ABSTRACT

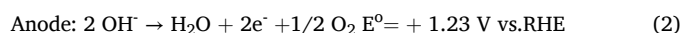
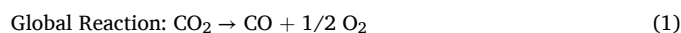
Electroreduction of CO₂ to obtain fossil fuel-free energy products is a promising avenue reducing anthropogenic greenhouse gas emissions. Catalysts based on Au, Ag and Cu are frequently used. Others based on abundant and low-cost elements such as Zn also report catalytic activity. This work presents a scalable and simple synthesis method of catalysts based on ZnO structures by a controlled thermal decomposition process of Zinc acetate dehydrate. An in-depth study of how modifications of synthesis parameters may affect the final performance of the material as electrocatalyst in CO₂RR is studied. It has been found that higher values of faradaic efficiency to CO evolution were found for samples synthesised at higher temperatures and higher heating ramp, reaching 69 % at -0.8 V vs RHE. It is of great importance to control over the parameters of the thermal decomposition process as they can greatly affect the final catalytic behaviour of the sample.

1. Introduction

Humanity's intensive exploitation of fossil fuels has brought our ecosystem to the brink of progressive degenerative change. As its increasingly severe consequences on the global climate manifest themselves year after year, it is a challenge to curb anthropogenic greenhouse gas emissions and accelerate the transition of modern society towards a more sustainable and circular economy with fossil fuel-free energy [1]. The efficient use of CO₂ as a useful feedstock plays a key role in bringing this vision closer to reality. Indeed, CO₂ capture and utilization strategies are currently seen as one of the promising energy solutions to achieve decarbonization targets. Thus, combining renewable sources with carbon dioxide recycling from various sources could generate sustainable products with a low carbon footprint [2–6].

Depending on the strategies developed, the conversion of CO₂ into industrial products involves different steps and reactions [7]. Various techniques are employed for CO₂ conversion, including electrochemical

reduction, thermochemical processes, and bio-electrochemical methods [8]. These processes can yield a range of useful products such as formic acid, methanol, hydrocarbons, and syngas [9]. Photocatalytic conversion, utilizing sunlight to produce hydrocarbon fuels, is also being explored [10]. Catalytic hydrogenation can produce methanol, methane, and hydrocarbons via Fischer-Tropsch synthesis [11]. Among the most important routes currently studied is electrochemical route [12], where the reduction of CO₂ into products such as CO is carried out using electrochemical devices to subsequently transform them into hydrocarbon chains through different catalytic reactions. CO is used in a variety of industries for a wide range of applications, including metal fabrication, chemicals, steel, pharma and biotechnology or electronics [13–15]. The electrochemical reduction reactions of CO₂ (CO₂RR) to CO can be observed in Eq. (1)–(3).



* Corresponding author.

E-mail address: rosero@icv.csic.es (N.C. Rosero-Navarro).

<https://doi.org/10.1016/j.oceram.2024.100733>

Received 26 June 2024; Received in revised form 10 December 2024; Accepted 24 December 2024

Available online 28 December 2024

2666-5395/© 2025 The Authors. Published by Elsevier Ltd on behalf of European Ceramic Society. This is an open access article under the CC BY-NC-ND license (<http://creativecommons.org/licenses/by-nc-nd/4.0/>).

Cathode: $\text{CO}_2 + \text{H}_2\text{O} + 2\text{e}^- \rightarrow \text{CO} + 2\text{OH}^-$ $E^\circ = -0.11$ V vs.RHE (3)

These processes are developed under alkaline conditions, as it is shown in Eqs. (2) and (3), which favour the dissolution of CO_2 in the electrolyte. Moreover, on the cathode side, with the formation of OH^- groups, the activity tends to increase with those conditions.

Notably, despite the equilibrium potential for CO_2 reduction to CO is low (-0.11 V vs RHE at $\text{pH} = 7$), a higher overpotential is typically required to overcome the sluggish reaction kinetics. The high overpotential would also cause an enhanced hydrogen evolution reaction (HER), competing with the CO_2RR , which lowers the CO selectivity. Therefore, the development of effective electrocatalysts is highly critical to reduce the overpotential and suppress HER to achieve high selectivity and activity in CO_2RR . The overpotential for the reduction of CO_2 to CO depends on several factors, such as cathode material, electrolyte and experimental conditions. The overpotential for the reduction of CO_2 to CO usually varies between 0.2 V and 1.0 V above the thermodynamic potential [16]. Catalysts such as gold (Au) and silver (Ag) are known to have relatively low overpotentials for CO production, around 0.3 V - 0.5 V [17].

The rational design of highly efficient electrocatalytic materials aims to reduce overpotentials and to achieve sufficient selectivity and conversion, trying to avoid the formation of several competitive by-products and low-yield reactions during the process. Precious metals such as gold, silver, platinum and their derivatives have been widely used in CO_2RR with the generation of products such as carbon monoxide, hydrogen, formic acid, ethylene and others [18–21]. However, their high cost limits their large-scale application. Among the various CO_2RR products, only CO and HCOOH production have achieved remarkable selectivity close to 100 %, showing the great potential for industrial application. Au-based catalysts demonstrate high selectivity, with Ag@Au core-shell nanowires achieving nearly 100 % Faradaic efficiency (FE) for CO production [22]. Hierarchically, nanoporous Au-Ag shells exhibit enhanced current density and CO FE compared to Au and Ag nanoparticles, highlighting the importance of mass transport within porous structures [23]. First-principles calculations reveal that the catalytic activity and selectivity of Ag and Au nanoparticles depend on various reaction sites, including low-index surfaces, edge sites, and corner sites. The size effect is crucial for nanoparticle corner sites, with 309-atom or larger nanoparticles recommended for accurately describing realistic metal nanocatalysts [24].

On the other hand, electrocatalysts based on elements such as cobalt, which have also proven to be efficient for CO_2RR [20], may be difficult to make available, presenting a geopolitical controversy. For this reason, the development of electrocatalysts based on metals that are more accessible in terms of availability, technology and cost represents a priority research challenge, including materials derived from elements such as Cu, Bi, Ni, Fe and Zn. In recent years, electrocatalysts based on metal oxides have gradually increased their interest in the community due to their promising values of FE and selectivity in the CO_2RR , although their stability is still a problem to be solved. Their use indicates an improvement in the adhesion of the CO_2 gas molecule itself to the electrode surface, facilitating the interaction and combining the competitive hydrogen evolution reaction (HER) given in the electrolyte of the system itself, resulting in an improvement of the selectivity towards products such as CO of the CO_2RR itself [25]. In addition, metal oxides can act in the stabilisation of intermediate species of CO_2RR products [26]. The selectivity of metal electrodes for CO formation follows the order $\text{Au} > \text{Ag} > \text{Cu} > \text{Zn}$, attributed to the stabilization of CO_2 intermediates on the electrode surface [27].

Zinc oxide is reported as an electrocatalyst with properties in CO_2RR [28], demonstrating their potential for selective product formation. The initial structure of ZnO and the electrolyte medium significantly influence the catalytic selectivity [29], according to different structures of this compound, including different routes in their synthesis or surface modifications among other, a wide range of FE for CO production in

CO_2RR can be observed, reported from 20 to 80 % [30–32]. Electrochemical reconstruction of ZnO materials can produce efficient CO_2 -to-CO catalysts, with >90 % selectivity and high stability [33]. Alloying ZnO with other metals, such as silver, can enhance activity and selectivity for further reduced products like methane and methanol, as well as changes in factors such as pressure, pH, and temperature may affect reaction efficiency [34]. These studies highlight the versatility of ZnO-based materials in CO_2 reduction, offering promising avenues for developing selective catalysts for various valuable products.

Inspired by the potential of the ZnO-based electrocatalysts, this work proposes the preparation of ZnO structures by a simple synthesis procedure based on thermal decomposition that provides practical benefits in the field of application as a low-cost, scalable, easy and quick methodology in industrial terms, as well as being an eco-friendly alternative to the conventional powerful electrocatalyst used in this field. For this purpose, thermal treatment used to obtain ZnO electrocatalysts is studied in depth, as well as their effect on CO_2RR electrocatalytic activity. Despite the simplicity of the synthesis to obtain ZnO-based materials by thermal decomposition, the selection of temperature and heating ramp significantly changes their physicochemical properties and electrocatalytic performance. For instance, FE for CO production varies from 11 % to 69 % by ZnO electrocatalysts obtained at 300 °C and 500 °C, respectively.

2. Experimental section

2.1. Materials

Zinc acetate dihydrate ($\text{Zn}(\text{CH}_3\text{CO}_2)_2 \cdot 2\text{H}_2\text{O}$, 98 % of purity, Sigma-Aldrich) was used as a main precursor in obtaining the ZnO structures without further purification.

2.2. Synthesis of ZnO electrocatalysts by thermal decomposition

The synthesis was based on the reported procedure [35]. Briefly, 0.5 g of Zinc acetate dihydrate, previously ground and sieved (500 μm), is heat treated in a low-cylindrical quartz crucible with 2 cm diameter, being the interface between the zinc acetate and gas the entire surface of the crucible. The synthesis is developed under an stagnant air atmosphere with a relative humidity of 54 % for 3 h, providing an oxidising atmosphere to facilitate the removal of residual carbon products. Several experiments were carried out at different temperatures (300 °C, 400 °C, 450 °C, 500 °C). Two heating ramps (0.7 °C/min and 5 °C/min) were selected for each experiment. The samples are designated as ZnO-xxx-y, where xxx is the temperature of synthesis in °C and y is the heating ramp in °C/min. Thus, sample ZnO-300-07 refers to ZnO synthesised from zinc acetate subjected to 300 °C with a heating ramp of 0.7 °C/min.

2.3. Preparation of the ZnO-loaded carbon paper as a working electrode

The ZnO structures-loaded carbon sheet was prepared by the following procedure. First, 2 mg of synthesised ZnO powders, 2 mg of the electronic conductive aid (Acetylene Black), 30 μL of the binder (5 wt% Anion exchange resin in propanol solution), and 270 μL of ethanol as solvent were mixed by grinding, resulting in a viscous black ink. 100 μL of the obtained mixture was deposited onto a carbon paper (TGP-H-090) by drop casting. The coating area was 1 cm^2 with a 1 cm square shape. Moreover, a blank electrode was prepared without the addition of the catalyst to the ink as a reference.

2.4. Physicochemical characterisation

A TG-DTA test with a SDT Q600 TA instrument (USA) was performed on the precursor zinc acetate dihydrate under an air atmosphere with a heating ramp of 2 °C/min from room temperature up to 500 °C.

The crystalline structure of the ZnO powders was determined by X-

ray diffraction (XRD), using *D8 Advance* (Bruker, USA) under CuK α radiation equipped with a lynx eye device for the simultaneous acquisition of diffractions at an interval of 3 ° (2 θ) in a range of 20–70 ° and a measurement step of 0.04. The diffractograms were analysed with the HighScore Plus software.

FT-IR spectroscopy was performed in a *Bruker Vertex spectrometer* equipped with an *MCT* (mercury cadmium telluride) *cryo-detector*. All the spectra were collected in the 4000–650 cm⁻¹ range with a resolution of 2 cm⁻¹ and an average of 32 scans. Before the analysis, the samples in form of self-supported pellets were inserted in a home-made quartz cell to undergo an activation procedure, which consists of heating in vacuum at 500 °C for 3 h using a 0.7 °C/min temperature ramp. Right after, 40 mbar of O₂ was dosed into the cell and left for 20 min at 500 °C before evacuating and repeating again the procedure. To get information about the nature of the active sites in the samples, approximately 25 mbar of CO were dosed to the ZnO-300-07 and ZnO-500-07 samples after the activation procedure. The cell was cooled down with liquid nitrogen until reaching a nominal temperature of 77 K, at which the interaction of CO with the acid sites of the samples are enhanced. Finally, different spectra were collected during gas expansions until all CO was desorbed.

The Specific Surface Area (SSA) of each sample was determined applying the Brunauer–Emmett–Teller (BET) equation in the 0.05 < p/p_0 < 0.3 range on the N₂ adsorption isotherms performed at 77 K by means of a Micromeritics *ASAP 2020* sorption analyzer. Prior to the measurement, all the samples were degassed under strict vacuum conditions (6.67·10⁻³ mbar) at room temperature for 20 h

Scanning electron microscopy (SEM) observation using a field emission scanning electron microscope (*FE-SEM Hitachi S-4700*, Japan), as well as Brightfield transmission electron microscopy (BFTEM) and electron diffraction (ED) on a *ThermoFisher Tecnai G2* microscope operated at 200 kV and equipped with a *Gatan US1000XP CCD* camera were used to characterize the morphology of ZnO powders and check for crystallinity. In addition, High-angle annular dark-field scanning transmission electron microscopy (HAADF-STEM) and STEM-Energy dispersive X-ray analysis (STEM-EDX) analysis were performed on a *ThermoFisher probe corrected Titan microscope* operated at 300 kV and equipped with a *Super X-detector* system. Elemental maps were acquired with a minimum duration of 20 min.

2.5. Electrocatalytic characterization

Electrochemical study was performed in H-type cell to determine the electrocatalytic behaviour of the ZnO catalysts in CO₂RR, following a reported procedure [36]. Briefly, a three-electrode setup was used, in which the ZnO-loaded carbon sheet, a platinum wire electrode (*CE-100A*, EC FRONTIER Co., Ltd.), and Ag/AgCl electrode (3.0 M KCl, *BAS Inc.*) were used as working, counter, and reference electrodes, respectively. The cathodic compartment and anodic compartment were separated by an anion exchange membrane (AEM) to avoid the unexpected influence of the oxidation reaction taking place on the counter electrode. A CO₂-saturated 0.10 M aqueous KHCO₃ solution (pH = 7.0) was used as the electrolyte. The CO₂ gas flowed with 20 mL/min flow rate and 0.10 MPa inlet pressure to the cathodic compartment, and the catholyte solution was stirred at 600 rpm. Under the above conditions, CO₂ electroreduction for 30 min was performed by applying a range of voltage with an electrochemical analyser (*SP-200*, Biologic). Gas-phase products were detected by gas chromatography techniques (*GC-2014*, Shimadzu Corp.; carrier gas: nitrogen, flow rate: 10 mL/min, pressure: 53.2 kPa, vaporization chamber temperature: 120 °C) by collecting gas for 10 min. For the detection of hydrogen (H₂), *Molecular Sieve 5A* (GL Sciences Inc.; column temperature: 50 °C, injected sample volume: 1 mL) and a thermal conductivity detector (*TCD*, Shimadzu Corp.; detector temperature: 120 °C) were used. For the detection of CO, *PoraPak N* (GL Sciences Inc.; column temperature: 50 °C, injected sample volume: 1 mL) a flame ionization detector (*FID*, Shimadzu Corp.; detector temperature: 120 °C) was used.

The evaluation of the catalytic activity of CO₂RR was carried out through a potentiostatic measurement, where the current density was determined by applying point voltage values between –0.6 V and –1.4 V against the reference hydrogen electrode (RHE). The electrode potentials in the study are converted to the reversible hydrogen electrode (E_{RHE}) or the standard hydrogen electrode (E_{SHE}) according to the following equations:

$$E_{RHE} = E_{SHE} + 0.059 \times pH \quad (4)$$

$$E_{SHE} = E_{Ag/AgCl} + 0.222 \quad (5)$$

Simultaneously, the gaseous products of the reaction were collected for 15 min by applying the specific potential between –0.6 V and –1.4 V vs. RHE. From the gas chromatographic analysis, the (FE) of the system in the evolution of CO and H₂, calculated from the expression (6) [37].

$$FE = (2VprF)/(IRT) \quad (6)$$

Where V is the volumetric concentration of CO or H₂ in the gas produced by the cell during the reaction. I (in mA) is the average current during the reaction, and r is the CO₂ flow rate (m³ s⁻¹) at room temperature and pressure. For the other constants in the formula, p is 1.013 × 10⁵ Pa, F is 96,485 C mol⁻¹, R is 8.3145 J mol⁻¹ K⁻¹, and T is 298 K. All potentials and voltages in this work were evaluated without iR compensation.

3. Results and discussion

The physicochemical characterisations of ZnO samples obtained by the modification of the synthesis temperature are shown below, followed by the results obtained in the electrocatalytic test for each of them, showing the differences in their behaviour as electrocatalysts in CO₂RR.

3.1. Physicochemical characterization

The TG-DTA of zinc acetate dihydrate is shown in Fig. 1, including the percentage weight loss of the compound (W), the first derivative curve of the percent weight loss (dW) (DTG) and heating flow (HF) (heat power registered per unit mass). The percent weight loss curve shows the dehydration of the material up to approximately 100 °C. Later, a mass loss of approximately 68 % of the initial mass takes place up to 285 °C, associated with the complete decomposition of zinc acetate to zinc oxide, which remains stable up to 500 °C. These thermal changes are also corroborated in the DTG curve with two main peaks centered at 85 °C and 285 °C, respectively. This latter one is broader and exhibits a shoulder at lower temperatures (approximately 230 °C). The heating flow curve shows associated endothermic peaks of the process of dehydration and zinc acetate decomposition. Particularly, the presence of three endothermic peaks centred between 240 °C and 280 °C, corresponding with the chemical transformation of zinc acetate to zinc oxide, suggests the development of several simultaneous processes or reactions during the thermal decomposition, coinciding with the behaviour observed in the DTG curve. Both facts are associated with a complex mechanism for the elimination of acetate-derived compounds to result in the final zinc oxide. The reactions carried out during the thermal decomposition process of zinc oxide have been previously reported, Eqs. (7)–10 (under O₂ conditions) [35]:



Multiple endothermic peaks (DTG profile) observed during the

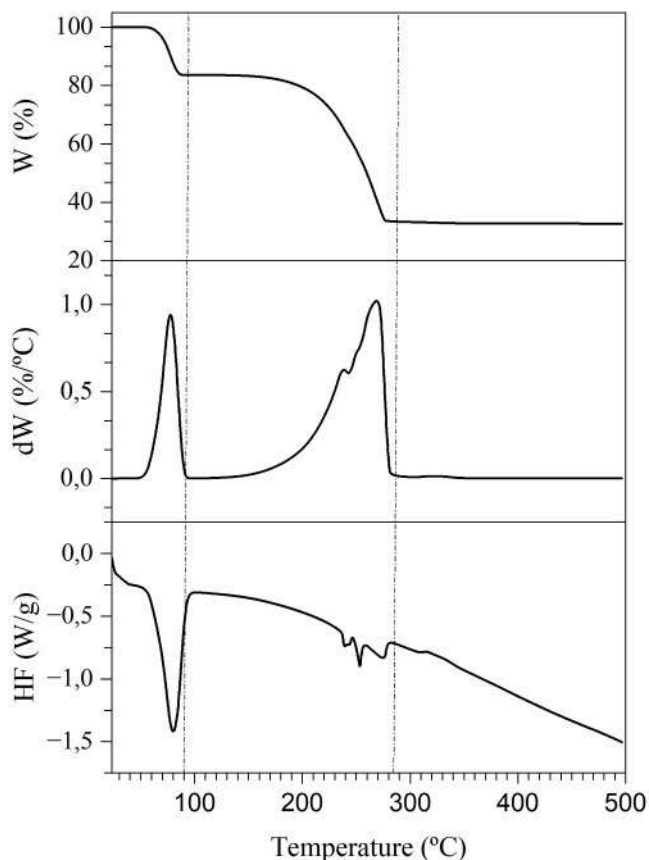


Fig. 1. TG-DTA of zinc acetate dihydrate up to 500 °C, including variation in weight (W), first derivate of weight (dW) and heating flow (HF).

thermal decomposition of zinc acetate around 250 °C can be related to possible simultaneous reactions, which could include the partial decomposition of acetate groups and the sublimation of dehydrated acetate species ($\text{ZnO}_4(\text{CH}_3\text{COO})_6$) [38]. Nevertheless, no mass loss was detected at temperatures higher than 285 °C, confirming that the nucleation and formation of zinc oxide occur from and at temperatures above that. Therefore, the heat treatment of zinc acetate dihydrate to form ZnO electrocatalysts was carried out at higher temperatures than 285 °C.

For the reference sample synthesised at 300 °C with a ramp of 0.7 °C/min, the final amount of product obtained after synthesis was compared with the theoretical amount to be obtained according to the thermal decomposition reactions of zinc acetate dihydrate proposed. This resulted in a yield of 77 %. The difference between the theoretical and experimental yield may be due to the fact that the totally amount of product obtained is not ZnO, the appearance of residual intermediate phases such as carbonate groups or that the starting precursor has absorbed molecules such as water or CO_2 , all of which are far from the theoretical ratio suggested. It should be noted that yield reaction was calculated considering the theoretical reactions of Eqs. (7)–10, which may differ slightly from what occurred in this experiment, as they could do not be following the same step-by-step conversion processes.

XRD patterns of ZnO obtained at different temperatures with a heating ramp of 0.7 °C/min are shown in Fig. 2. Table 1 summarizes the lattice parameters and cell volume obtained from XRD patterns. Basically, identical XRD patterns were identified for ZnO obtained at different temperatures and peaks coinciding with ZnO crystal phase (space group $P63mc$). Moreover, the lattice parameters and cell volume are in good agreement with reference parameters from Inorganic Crystal Structural Database (ICSD) file number 98–004–1488. The hexagonal crystal system was verified with a preferential direction of growth

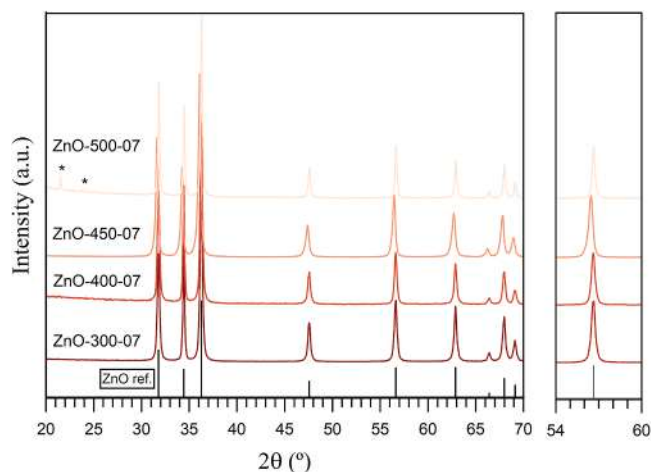


Fig. 2. XRD patterns of ZnO synthesised at 0.7 °C/min and different temperatures, including the ZnO reference pattern (denoted as ZnO ref.) which corresponds to ICSD 98–004–1488 file and * denoting secondary phases.

Table 1

Characteristic parameters of cell units from ZnO synthesised at different temperatures and 0.7 °C/min and ZnO reference pattern (denoted as ZnO ref.) which corresponds to ICSD 98–004–1488 file.

Sample	a (Å)	b (Å)	c (Å)	Cell Volume (Å ³)
ZnO-300-07	3.2513(2)	3.2513(2)	5.2093(3)	47.69
ZnO-400-07	3.2511(8)	3.2511(8)	5.2093(3)	47.68
ZnO-450-07	3.2590(1)	3.2590(1)	5.2270(4)	48.09
ZnO-500-07	3.2496(2)	3.2496(2)	5.2063(9)	47.61
ZnO ref.	3.2490	3.2490	5.2070	47.60

developed in the (101) planes ($2\theta = 36.26^\circ$). Secondary phases were observed in the XRD pattern (weak peaks at $2\theta = 21.35^\circ$ and $2\theta = 23.65^\circ$) of the ZnO-500–07 sample. Those phases are recognized as distinct from the main ZnO phase or main peaks of the precursor of the synthesis [39]. Partial decomposition of ZnO could be a reason of these peaks. The peaks of the diffraction patterns shift to lower 2θ with an increase in the temperature of the synthesis (exception 500 °C) coinciding with a slight increase in cell volume (Table 1). Deviation of the tendency of ZnO-500–07 sample can be related to local heterogeneity of ZnO crystals and deformation Zn–O bonds [40,41], accomplished of the presence of secondary phases. Nevertheless, all ZnO samples show a high crystallinity with a negligible variation in their parameters. The trends observed for the syntheses performed at a ramp of 0.7 °C/min were also verified in the samples synthesised with a heating rate of 5 °C/min (Fig. A.1 and Table A.1), which confirms that ZnO with high crystallinity can be easily prepared at temperature higher than 300 °C, as expected from TG-DTA analyses, despite the identification of a few secondary phases as in sample ZnO-500–07.

Fig. 3 shows the morphology of ZnO synthesised at different temperatures using a heating ramp of 0.7 °C/min and corresponding surface area values. Clear and defined rod-shaped particles were observed for ZnO-300–07, while less defined rods interspersed with nanoparticles were observed for ZnO-400–07. Spherical-type nanoparticles were observed for ZnO-450–07 and ZnO-500–07. The formation of well-defined rods observed in ZnO-300–07 achieves sizes between 400 nm to around 1.5 μm , while the ZnO-400–07 rod-shaped particles were smaller, from 110 nm to 760 nm, with nanoparticles with sizes between 20 and 200 nm. Small agglomerated particles without a clear morphology with sizes around 50 nm were also observed in ZnO samples obtained at lower temperatures (300 °C and 400 °C). Spherical particles, with sizes from 30 nm to less than 200 nm, were obtained in ZnO-450–07 and ZnO-500–07. On the other hand, the surface area (Fig. 3e) of

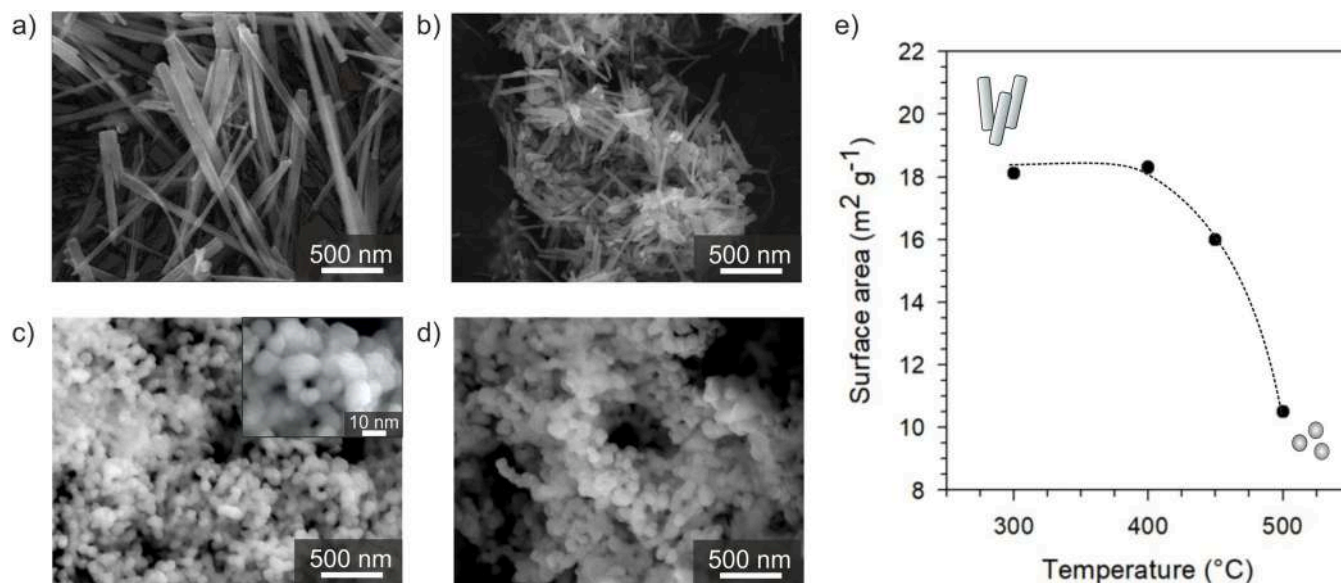


Fig. 3. SEM images of a) ZnO-300-07, b) ZnO-400-07, c) ZnO-450-07, d) ZnO-500-07 and e) corresponding surface area.

obtained ZnO samples decreases with the temperature used for thermal decomposition, varying from circa of $18 \text{ m}^2 \text{ g}^{-1}$ for nanorod particles in ZnO-300-07 to $10 \text{ m}^2 \text{ g}^{-1}$ for spherical-type nanoparticles in ZnO-500-07. Agglomeration of particles was also observed in ZnO sintered at higher temperatures (Inset Fig. 3c) that could contribute to the drop of the surface area value in the ZnO obtained at higher temperatures.

In contrast, ZnO synthesised at different temperatures with a higher heating ramp of $5 \text{ }^\circ\text{C}/\text{min}$ did not show at any temperature the formation of rod shapes or elongated particles, Fig. A.2. ZnO-300-5, ZnO-400-5, ZnO-450-5, ZnO-500-5 exhibited predominantly rounded particles with sizes from 20 nm to 200 nm, with a few elongated particles only observed in ZnO-300-5 sample, and surface areas around $10 \text{ m}^2 \text{ g}^{-1}$. The apparent change of ZnO morphology with temperatures and heating ramps suggests that the enlarged nanorods are mainly obtained when a low heating ramp is used and spherical-type particles tend to form by increasing the temperature or heating ramp. This type of behaviour can be explained by the formation of acetic acid produced during thermal decomposition, that causes a local pH decreasing locally, in the reaction sites, and promotes the formation of rod-shaped particles. An increase in the heating ramp or synthesis temperature produces a higher evaporation rate of this acetic acid, which can be related to the endothermic peaks observed in the TG-DTA. This phenomenon neutralises the local pH more rapidly, promoting the formation of nanoparticles instead of rod-shaped particles [39]. This premise justifies the fact that, in this study, the synthesis with a lower ramp and temperature ($0.7 \text{ }^\circ\text{C}/\text{min}$ and $300 \text{ }^\circ\text{C}$) presents the most defined morphology of rod-shaped particles, while as the temperature and/or ramp increases, this definition is lost gradually until reaching a formation of spherical particles in their entirety, which is seen with a ramp of $0.7 \text{ }^\circ\text{C}/\text{min}$ from an applied temperature of $450 \text{ }^\circ\text{C}$ and with a higher ramp, $5 \text{ }^\circ\text{C}/\text{min}$ from $400 \text{ }^\circ\text{C}$ applied.

Fig. 4 shows additional microstructure information for ZnO-300-07 sample. Rod shaped characteristic particle morphology was clearly verified. In addition, small aggregated particles, with no apparent shape, were also observed (Fig. 4b, agglomerated particle close to main rod-shaped particle). Diffraction analyses performed on these different particles confirmed crystalline diffraction for the elongated needle particles (Fig. 4c-d) and revealed no diffraction pattern for agglomerated small particles, which indicates that these particles are amorphous.

The elemental analyses confirmed the presence of zinc and oxygen and the absence of other elements, with a roughly 50–50 percent ($\pm 3 \%$) distribution of Zn and O, confirming the basic composition of ZnO. The

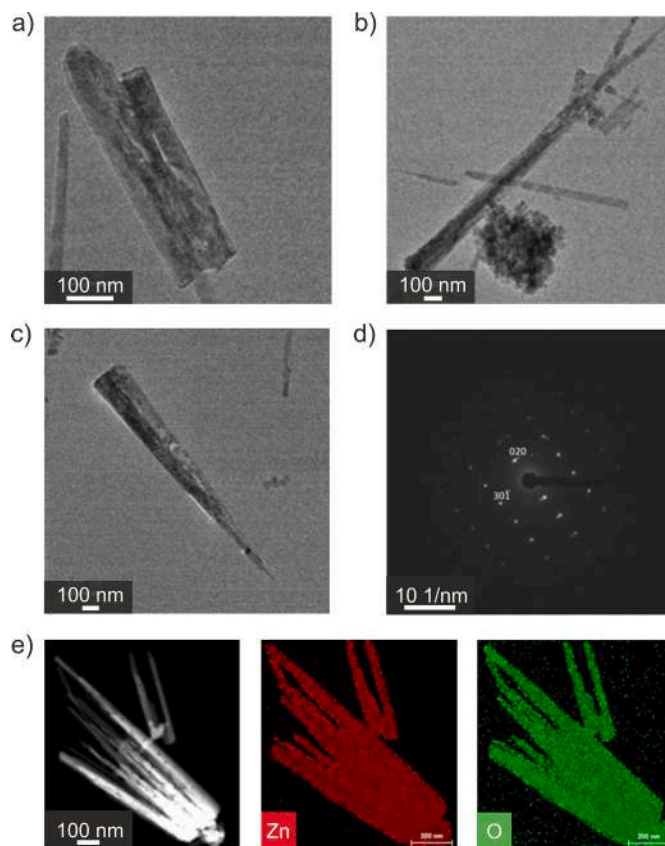


Fig. 4. a) - c) BFTEM images and d) corresponding electron diffraction pattern from the particle in c). e) Zn and O elemental mappings of ZnO-300-07 particles.

elemental composition of smaller amorphous particles consists of slightly oxygen-rich ZnO. Based on microstructure analyses, ZnO by thermal decomposition can achieve high crystallinity with a rather homogenous elemental distribution from low temperatures of $300 \text{ }^\circ\text{C}$. The amorphous character can be associated with the formation mechanism of ZnO from the thermal decomposition of zinc acetate.

FTIR spectra of the as-synthesised and activated ZnO-300-07 and ZnO-500-07 samples are shown in Fig. A.3. In the high wavenumber region ($3700\text{--}3000\text{ cm}^{-1}$) the as-synthesised samples show a broad band due to the hydroxyl-stretching vibrations of water molecules, which are almost fully removed during the activation procedure in vacuum, except for some residual OH groups in the $3730\text{--}3330\text{ cm}^{-1}$ spectral range whose high thermal stability suggests their localization in some defective sites [42]. In the low wavenumber region ($1000\text{--}650\text{ cm}^{-1}$) the characteristic M-O ($M=\text{Zn}$) lattice vibrations can be observed [43]. In the $1800\text{--}1200\text{ cm}^{-1}$ spectral range several overlapping bands can be identified. After the activation procedure, the bands within this spectral range undergo different changes: the shoulder in the $1700\text{--}1600\text{ cm}^{-1}$ range disappears due to erosion of the HOH bending vibrations ($\sim 1640\text{ cm}^{-1}$), while two intense bands in the $1600\text{--}1470$ and $1470\text{--}1270\text{ cm}^{-1}$ range become more evident. Those latter bands are probably related to the formation of carbonate species located in some strong defective sites resistant to activation procedure [42]. However, in addition to those bands, the characteristic CO_2 ν_3 asymmetric stretching vibration at 2340 cm^{-1} and two bands at around 2925 and 2855 cm^{-1} corresponding to C-H stretching vibrations can be observed in both samples before and after the activation. The appearance of all those bands suggests the presence of intermediate product of the thermal decomposition process. Indeed, the presence of carbon-based materials is not surprising since the thermal decomposition involves the elimination of acetate-derived compounds as described in Eqs. (7) to 11. Furthermore, in addition to carbonate-like species, $\nu_a\text{ COO}^-$ and $\nu_s\text{ COO}^-$ vibrational modes of the carboxyl groups of acetate species were also reported in the $1800\text{--}1200\text{ cm}^{-1}$ spectral region, which may further indicate the presence of some intermediate product of the thermal decomposition process [44]. The presence of those bands suggests that some species coming in part from the decomposition synthesis of zinc acetate could remain in the final ZnO composition even after the thermal decomposition at temperatures above $300\text{ }^\circ\text{C}$ (verified in TG-DTA analysis). The difficulty of full removal of carbon-based compounds during synthesis, could also justify the amorphous character of some particles seen in TEM.

To study the active sites present in ZnO-300-07 and ZnO-500-07 samples, CO, acting as weak Lewis base, was put in contact in doses on the activated samples (Fig. 5). Both samples show a broad peak characterized by a roto-vibrational profile suggesting the presence of CO in the gas phase. At high CO coverage, a maximum centred around 2148 cm^{-1}

cm^{-1} is observed, probably due to CO species adsorbed on residual hydroxyl groups. This interaction usually also causes some mutations in the OH stretching region, but these are not easily detectable due to the low intensity of the signals (Fig. A.4). On the other hand, at lower coverages, a broader band appears in the $2175\text{--}2155\text{ cm}^{-1}$ spectral region, associated with CO adsorption on Zn^{2+} ions belonging to different faces. A clear identification of the main bands is not straightforward due to the low intensity of the signals and the presence of several overlapping bands. The low intensities of these bands and the prevalence of CO in the gas phase at higher pressures may be related to the presence of different residual intermediate species that prevent the full accessibility of these sites.

3.2. Electrocatalytic characterization

Fig. 6 shows Faraday Efficiency values for H_2 , CO (FE_{H_2} and FE_{CO} , respectively) and other gas products obtained by gas chromatography from the cathodic compartment in the H-type electrochemical cell for ZnO samples synthesised at different temperatures with a heating ramp of $0.7\text{ }^\circ\text{C}/\text{min}$. The current density (j) for the cathodic reaction is also included for each sample. High FE_{CO} results are observed between potential ranges of $0.8\text{--}1.2\text{ V}$ for all samples. Depending on the temperature used for the preparation of ZnO by thermal decomposition, the evolution of carbon monoxide is greater at the higher temperature used, while the evolution of hydrogen is lower. FE_{CO} for ZnO-300-07, ZnO-400-07, ZnO-450-07 and ZnO-500-07 achieves 41 %, 46 %, 56 % and 62 % at -0.8 V vs. RHE, respectively. FE_{CO} for ZnO-450-07 increases up to 63 % at -1 V vs. RHE. Regarding current density, j_{total} achieves -10 mA cm^{-2} at -1 V vs. RHE for all samples and the largest partial current densities of CO around -6 mA cm^{-2} at -1 V vs. RHE are obtained for ZnO-450-07 and ZnO-500-07. On the other hand, FE_{H_2} for ZnO-300-07, ZnO-400-07, ZnO-450-07 and ZnO-500-07 reaches 24 %, 23 %, 12 % and 17 % at -0.8 V vs. RHE, respectively. ZnO-450-07 showed a highest CO evolution maintaining a low H_2 evolution at -0.8 V to -1.4 V vs. RHE which suggest a more selective reaction.

The electrocatalytic performance of ZnO samples synthesised at different temperatures with a heating ramp of $5\text{ }^\circ\text{C}/\text{min}$ (Fig. A.5) showed similar tendency to those observed in the ZnO obtained with a low heating ramp of $0.7\text{ }^\circ\text{C}/\text{min}$. A decrease of FE_{CO} is obtained at lower synthesis temperatures ($300\text{ }^\circ\text{C}$ and $400\text{ }^\circ\text{C}$) reaching values of around

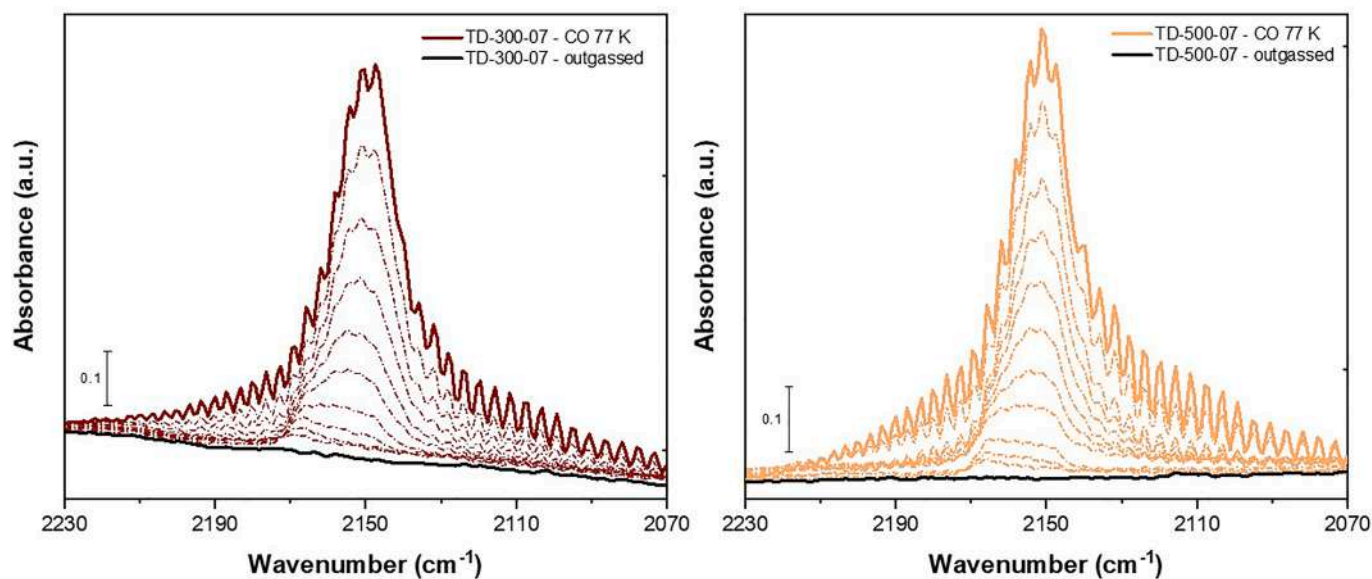


Fig. 5. IR spectra of CO adsorption at 77 K on activated ZnO-300-07 and ZnO-500-07 samples, recorded at different CO coverages and reported in the CO vibrational modes region. Coloured spectra: maximum CO coverage (25 mbar). Dotted spectra: decreasing pressure steps. Black spectra: outgassing in vacuum until 10^{-3} mbar. A baseline correction and normalisation to the 990 cm^{-1} band was performed.

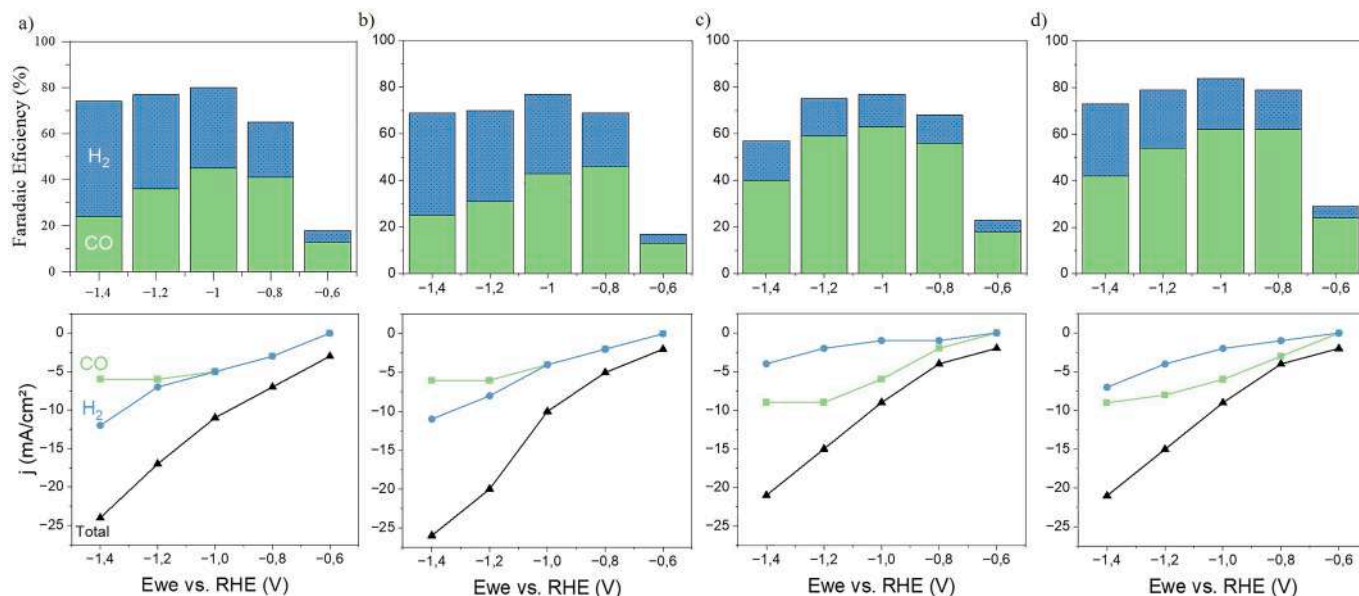


Fig. 6. FE values at different potentials and the respective current density obtained for a) ZnO-300-07, b) ZnO-400-07, c) ZnO-450-07, d) ZnO-500-07.

38 % at -1 V vs. RHE (-4 mA cm $^{-2}$) for ZnO-300-5 and 26 % at -1 V vs. RHE (-2 mA cm $^{-2}$) for ZnO-400-5. In contrast, a slight improvement in FE_{CO} is obtained at higher synthesis temperatures, reaching values of around 69 % at -1 V vs. RHE (-6 mA cm $^{-2}$) for ZnO-450-5 and 68 % at -1 V vs. RHE (-6 mA cm $^{-2}$) for ZnO-500-5. In any case, all the ZnO samples synthesised show an improvement in the FE_{CO} values at any of the potentials studied compared to the predominant H_2 evolution demonstrated by the carbon paper depositing an ink without ZnO. Furthermore, an improvement in the electrochemical activity of the processed working electrodes including ZnO is observed, since higher current densities reached at the same measured potential are achieved with respect to the carbon paper with ink in absence of ZnO catalyst (Fig. A.6). In addition, it must be taken into account that, from -1 V vs. RHE applied, the by-product produced is mostly H_2 which, although it is a competitive product for CO_2RR and CO production, is of great energetic interest, also forming syngas in its combination with the CO also produced [45]. More specifically, all the ZnO samples synthesized have presented an FE of almost 80 % or higher in the mixture of CO and H_2 , which is of great interest and opens the possibilities for further reactions in the energy sector.

In light of these results, it is evident that the CO_2RR electrocatalytic performance of ZnO materials is favoured when a high synthesis temperature is used. ZnO with high crystallinity was obtained from the complete decomposition of zinc acetate at temperatures of about 300 °C to 500 °C, resulting in morphologies that changed from rod-shaped particles to spherical-shaped particles. Even though the trend observed in FE_{CO} would suggest that major modifications observed in ZnO synthesised samples such as morphology play a key role in justifying the different performances, other differences among samples such as secondary phases observed at high synthesis temperatures (500 °C, verified by XRD, Fig. 2) or the presence of amorphous particles observed at low synthesis temperatures (300 °C, verified by BFTEM, Fig. 4) could be relevant to the final outcomes. Additionally, the possible presence of carbonaceous-derived products in ZnO synthesised samples (verified by FT-IR, Fig. 5, Fig. A.3 and Fig. A.4) could further affect the different electrocatalytic performance of ZnOs. Particularly, if this remaining carbon is reactive and forms other products on the surface, affecting active sites, or desired reactants (CO_2 -to-CO) trapped during the catalysts process. Therefore, the selection of temperature is a critical parameter for the synthesis of electrocatalysts by thermal decomposition, since it is these parameters that determine the morphology,

crystallinity, possible secondary and/or amorphous phases and the presence of carbonaceous products remaining in the final ZnO synthesised, and it is the synergy of these properties that makes it possible to achieve a better performance in the CO_2RR .

Recent studies have demonstrated significant improvements in the electrochemical reduction reaction of CO_2 to CO using improved noble metal electrocatalysts with new synthesis protocols. Oxide-derived nanostructured silver electrocatalysts showed enhanced CO_2 reduction performance, achieving ~ 80 % FE for CO production at a moderate overpotential of 0.49 V [46]. Plasma-oxidized silver foils exhibited even higher efficiency, reaching over 90 % FE towards CO at -0.6 V vs. RHE [47]. This enhancement was attributed to the increased number of low-coordinated active sites created by the plasma treatment. Studies have demonstrated high FE for CO production, with 8 nm Au NPs achieving up to 90 % FE at -0.67 V vs RHE [48]. The shape and size of Au nanostructures significantly influence their catalytic performance, with Au trisoctahedrons exhibiting higher FE (88.80 %) compared to Au colloids (59.04 %) [49]. Surface functionalization of Au NPs with N-heterocyclic carbene ligands improved FE to 83 % and increased current density 7.6-fold compared to unfunctionalized Au NPs [50]. Additionally, hierarchically structured Au island catalysts prepared by oxygen plasma treatment achieved over 95 % FE for CO production [51]. These studies also highlight the importance of combination of size, shape, surface functionalization, and structural modifications in optimizing electrocatalysts for CO_2 reduction to CO.

On the other hand, Pt catalysts on gas diffusion electrodes under high pressure achieve 46 % FE for CO_2 reduction, producing methane (35 %) and ethanol (2.2 %) [52]. The energy conversion efficiency of CO_2 reduction to CO is highest with Au catalysts, while Pt shows advantages for overall energy conversion due to negligible activation energy [53].

Factors influencing efficiency include electrocatalyst type, reaction complexity, electrode surface treatment, electrolyte composition, and operating conditions such as current density and CO_2 pressure. Although the ZnO electrocatalyst studied in this paper has a moderate FE in the production of CO, ZnO-based materials are exciting alternatives in terms of cost, procurement, and practicality of synthesis, even at an industrial level. They are also becoming a promising option for future studies to improve them.

4. Conclusion

Practical, simple and economical synthesis of ZnO by thermal decomposition of zinc acetate dihydrate was studied using temperatures at 300 °C, 400 °C, 450 °C and 500 °C, and heating ramps of 0.7 °C/min and 5 °C/min. TG-DTA analysis of zinc acetate dihydrate suggests complete formation of ZnO and no further mass loss above 285 °C. XRD patterns confirmed ZnO formation with high crystallinity for all samples and presence of secondary phases in the higher synthesis temperature. Transmission electron microscopy analyses verified the formation of well-defined rod-shaped particles at low synthesis temperatures and heating ramps, as well as the formation of nanoparticles for high synthesis temperatures. Amorphous ZnO particles were also observed in materials synthesised at low temperatures. FT-IR revealed the presence of carbonaceous-derived products remaining in the powder samples that may affect the active sites in ZnO synthesised samples. The highest values of FE for CO evolution can be observed for the ZnO samples synthesised at high temperatures with a higher heating ramp. Faradaic efficiency FE values can vary from 62 % to 69 % at -1 V vs. RHE (-6 to -8 mA cm $^{-2}$) depending on synthesis temperature and heating ramp. Despite the results shown in this study being a simple synthesis method, it is of great importance to control the parameters of the thermal decomposition process as they can greatly affect the final catalytic behaviour of the sample.

CRediT authorship contribution statement

Elías Rodríguez-Jara: Writing – review & editing, Writing – original draft, Validation, Methodology, Investigation, Formal analysis, Conceptualization. **Margherita Cavallo:** Writing – review & editing, Writing – original draft, Validation, Methodology, Investigation, Formal analysis, Conceptualization. **Ryosuke Nakazato:** Writing – review & editing, Investigation, Formal analysis. **Matthias Quintelier:** Writing – review & editing, Investigation, Formal analysis. **Keeko Matsumoto:** Writing – review & editing, Investigation, Formal analysis. **Joke Hadermann:** Writing – review & editing, Supervision, Funding acquisition. **Jadra Mosa:** Writing – review & editing, Investigation, Formal analysis. **Francesca Bonino:** Writing – review & editing, Supervision, Project administration. **Kiyoharu Tadanaga:** Writing – review & editing, Supervision, Project administration. **Mario Aparicio:** Writing – review & editing, Supervision, Project administration. **Nataly Carolina Rosero-Navarro:** Writing – review & editing, Writing – original draft, Supervision, Resources, Project administration, Methodology, Funding acquisition, Conceptualization.

Declaration of competing interest

The authors declare that they have no known competing financial interests or personal relationships that could have appeared to influence the work reported in this paper.

Acknowledgements

The authors are grateful to JECS Trust for funding the visit of Elías Rodríguez Jara to University of Turin (Contract No. 2022325) and the visit of Margherita Cavallo to Institute of Ceramic and Glass (Contract No.2022339). This research was supported through 4AirCRAFT project under the strategic international cooperation between Europe (Horizon2020, No.101022633) and Japan Science and Technology Agency (JST) with reference number JPMJSC2102. MC and FB acknowledge support from the Project CH4.0 under the MUR program "Dipartimenti di Eccellenza 2023–2027" (CUP: D13C22003520001). N.C. R-N. acknowledge the financial support through the Ramón y Cajal grant No. RYC2020–029909-I of the Spanish State Research Agency and the IDEAL-Li Project (Ref. PIE - 2022AT009, Talent Attraction) of The Spanish National Research Council (CSIC).

Supplementary materials

Supplementary material associated with this article can be found, in the online version, at [doi:10.1016/j.oceram.2024.100733](https://doi.org/10.1016/j.oceram.2024.100733).

References

- [1] J.A. Pinilla, El problema Energético Mundial, *Energías Renovables y Cambio Climático*, *Energy Manag* (2019).
- [2] H. Wei, W. Liu, X. Chen, Q. Yang, J. Li, H. Chen, Renewable bio-jet fuel production for aviation: A review, *Fuel* 254 (2019) 115599, <https://doi.org/10.1016/J.FUEL.2019.06.007>.
- [3] J. Artz, T.E. Müller, K. Thenert, J. Kleinekorte, R. Meys, A. Sternberg, A. Bardow, W. Leitner, Sustainable Conversion of Carbon Dioxide: An Integrated Review of Catalysis and Life Cycle Assessment, *Chem. Rev.* 118 (2018) 434–504, https://doi.org/10.1021/ACS.CHEMREV.7B00435/ASSET/IMAGES/MEDIUM/CR-2017-004352_0047.GIF.
- [4] Z. Zhang, S.Y. Pan, H. Li, J. Cai, A.G. Olabi, E.J. Anthony, V. Manovic, Recent advances in carbon dioxide utilization, *Renew. Sustain. Energy Rev.* 125 (2020) 109799, <https://doi.org/10.1016/j.rser.2020.109799>.
- [5] C.G. Okoye-Chine, K. Otun, N. Shiba, C. Rashama, S.N. Ugwu, H. Onyeaka, C. T. Okeke, Conversion of carbon dioxide into fuels - A review, *J. CO2 Util.* 62 (2022) 102099, <https://doi.org/10.1016/j.jcou.2022.102099>.
- [6] G. Fiorani, W. Guo, A.W. Kleij, Sustainable conversion of carbon dioxide: The advent of organocatalysis, *Green Chem* 17 (2015) 1375–1389, <https://doi.org/10.1039/c4gc01959h>.
- [7] C. Kim, C.J. Yoo, H.S. Oh, B.K. Min, U. Lee, Review of carbon dioxide utilization technologies and their potential for industrial application, *J. CO2 Util.* 65 (2022) 102239, <https://doi.org/10.1016/J.JCOU.2022.102239>.
- [8] M.A. Shah, A.L. Shibiru, V. Kumar, V.C. Srivastava, Carbon dioxide conversion to value-added products and fuels: opportunities and challenges: a critical review, *Int. J. Green Energy* (2023), <https://doi.org/10.1080/15435075.2023.2281330>.
- [9] Inamuddin, A.M. Asiri, E. Lichtfouse, eds., Conversion of Carbon Dioxide into Hydrocarbons Vol. 1 Catalysis, 40 (2020). <https://doi.org/10.1007/978-3-030-28622-4>.
- [10] T.A. Saleh, Nanomaterials and hybrid nanocomposites for CO₂ capture and utilization: environmental and energy sustainability, *RSC Adv* 12 (2022) 23869, <https://doi.org/10.1039/D2RA03242B>.
- [11] G. Centi, E.A. Quadrelli, S. Perathoner, Catalysis for CO₂ conversion: a key technology for rapid introduction of renewable energy in the value chain of chemical industries, *Energy Environ. Sci.* 6 (2013) 1711–1731, <https://doi.org/10.1039/C3EE00056G>.
- [12] D. Graf, N. Monnerie, M. Roeb, M. Schmitz, C. Sattler, Economic comparison of solar hydrogen generation by means of thermochemical cycles and electrolysis, (2008). <https://doi.org/10.1016/j.jhydene.2008.05.086>.
- [13] H. Schulz, Short history and present trends of Fischer-Tropsch synthesis, *Appl. Catal. A Gen.* 186 (1999) 3–12, [https://doi.org/10.1016/S0926-860X\(99\)00160-X](https://doi.org/10.1016/S0926-860X(99)00160-X).
- [14] S.W. Ryter, A.M.K. Choi, Carbon monoxide: Present and future indications for a medical gas, *Korean J. Intern. Med.* 28 (2013) 123–140, <https://doi.org/10.3904/kjim.2013.28.2.123>.
- [15] K. Sobieraj, S. Steganta-Dąbrowska, G. Luo, J.A. Koziel, A. Białowiec, Carbon Monoxide Fate in the Environment as an Inspiration For Biorefinery Industry: A Review, *Front. Environ. Sci.* 10 (2022) 1–24, <https://doi.org/10.3389/fenvs.2022.822463>.
- [16] J. Lin, Y. Zhang, P. Xu, L. Chen, CO₂ electrolysis: Advances and challenges in electrocatalyst engineering and reactor design, *Mater. Reports Energy* 3 (2023) 100194, <https://doi.org/10.1016/J.MATRE.2023.100194>.
- [17] G. Leonzio, A. Hankin, N. Shah, CO₂ electrochemical reduction: A state-of-the-art review with economic and environmental analyses, *Chem. Eng. Res. Des.* 208 (2024) 934–955, <https://doi.org/10.1016/J.CHERD.2024.07.014>.
- [18] X. Zhu, J. Huang, M. Eikerling, Electrochemical CO₂ Reduction at Silver from a Local Perspective, *ACS Catal* 11 (2021) 14521–14532, <https://doi.org/10.1021/acscatal.1c04791>.
- [19] J.W. Vickers, D. Alfonso, D.R. Kauffman, Electrochemical Carbon Dioxide Reduction at Nanostructured Gold, Copper, and Alloy Materials, *Energy Technol* 5 (2017) 775–795, <https://doi.org/10.1002/ENTE.201600580>.
- [20] M. Abdinejad, A. Seifitokaldani, C. Dao, E.H. Sargent, X.A. Zhang, H.B. Kraatz, Enhanced Electrochemical Reduction of CO₂ Catalyzed by Cobalt and Iron Amino Porphyrin Complexes, *ACS Appl. Energy Mater.* 2 (2019) 1330–1335, <https://doi.org/10.1021/acsaem.8b01900>.
- [21] P.A. Christensen, A. Hamnett, A.V.G. Muir, N.A. Freeman, CO₂ reduction at platinum, gold and glassy carbon electrodes in acetonitrile. An in-situ FTIR study, *J. Electroanal. Chem.* 288 (1990) 197–215, [https://doi.org/10.1016/0022-0728\(90\)80035-5](https://doi.org/10.1016/0022-0728(90)80035-5).
- [22] J. Liu, Y. Wang, H. Jiang, H. Jiang, X. Zhou, Y. Li, C. Li, Ag@Au Core-Shell Nanowires for Nearly 100 % CO₂ to-CO Electroreduction, *Chem. Asian J.* 15 (2020) 425–431, <https://doi.org/10.1002/ASIA.201901550>.
- [23] W. Yang, L. Qian, P. Lei, J. Chen, X. Lu, T. Yu, H. Xiao, X. Zhou, B. Kathale, Active and selective CO₂ electroreduction on a hierarchically nanoporous Au-Ag shell, *Chem. Phys. Lett.* 753 (2020) 137563, <https://doi.org/10.1016/J.CPLETT.2020.137563>.
- [24] S. Back, M.S. Yeom, Y. Jung, Active Sites of Au and Ag Nanoparticle Catalysts for CO₂ Electroreduction to CO, *ACS Catal* 5 (2015) 5089–5096, <https://doi.org/10.1021/ACSCATAL.5B00462>.

- [25] P.K. Jiwan, S. Sultana, W.P. Wicaksono, Y. Einaga, Metal modified carbon-based electrode for CO₂ electrochemical reduction: A review, *J. Electroanal. Chem.* 898 (2021) 115634, <https://doi.org/10.1016/J.JELECHEM.2021.115634>.
- [26] S. Chu, P. Ou, P. Ghamari, S. Vanka, B. Zhou, I. Shih, J. Song, Z. Mi, Photoelectrochemical CO₂ Reduction into Syngas with the Metal/Oxide Interface, *J. Am. Chem. Soc.* 140 (2018) 7869–7877, <https://doi.org/10.1021/JACS.8B03067/ASSET/IMAGES/LARGE/JA-2018-03067X.0005.JPEG>.
- [27] Y. Hori, H. Wakebe, T. Tsukamoto, O. Koga, Electrocatalytic process of CO selectivity in electrochemical reduction of CO₂ at metal electrodes in aqueous media, *Electrochim. Acta* 39 (1994) 1833–1839, [https://doi.org/10.1016/0013-4686\(94\)85172-7](https://doi.org/10.1016/0013-4686(94)85172-7).
- [28] S. Ikeda, A. Hattori, M. Maeda, K. Ito, H. Noda, Electrochemical Reduction Behavior of Carbon Dioxide on Sintered Zinc Oxide Electrode in Aqueous Solution, *Electrochemistry* 68 (2000) 257–261, <https://doi.org/10.5796/ELECTROCHEMISTRY.68.257>.
- [29] K. Han, P. Ngene, P. de Jongh, Structure Dependent Product Selectivity for CO₂ Electroreduction on ZnO Derived Catalysts, *ChemCatChem* 13 (2021) 1998–2004, <https://doi.org/10.1002/CCTC.202001710>.
- [30] Z. Geng, X. Kong, W. Chen, H. Su, Y. Liu, F. Cai, G. Wang, J. Zeng, Oxygen Vacancies in ZnO Nanosheets Enhance CO₂ Electrochemical Reduction to CO, *Angew. Chemie* 130 (2018) 6162–6167, <https://doi.org/10.1002/ANGE.201711255>.
- [31] L. Xue, A. Zhang, J. Wu, Q. Wang, Y. Liu, Y. Zhao, S. Liu, Z. Liu, P. Li, S. Zeng, Surface modification and reconstruction of ZnO hollow microspheres for selective electroreduction of CO₂ to CO, *J. Alloys Compd.* 882 (2021) 160703, <https://doi.org/10.1016/j.jallcom.2021.160703>.
- [32] K. Han, P. Ngene, P. de Jongh, Structure Dependent Product Selectivity for CO₂ Electroreduction on ZnO Derived Catalysts, *ChemCatChem* 13 (2021) 1998–2004, <https://doi.org/10.1002/cctc.202001710>.
- [33] W. Luo, Q. Zhang, J. Zhang, E. Moiola, K. Zhao, A. Züttel, Electrochemical reconstruction of ZnO for selective reduction of CO₂ to CO, *Appl. Catal. B Environ.* 273 (2020) 119060, <https://doi.org/10.1016/J.APCATB.2020.119060>.
- [34] T. Hatsukade, K.P. Kuhl, E.R. Cave, D.N. Abram, J.T. Feaster, A.L. Jongorius, C. Hahn, T.F. Jaramillo, Carbon Dioxide Electroreduction using a Silver–Zinc Alloy, *Energy Technol.* 5 (2017) 955–961, <https://doi.org/10.1002/ENTE.201700087>.
- [35] C.C. Lin, Y.Y. Li, Synthesis of ZnO nanowires by thermal decomposition of zinc acetate dihydrate, *Mater. Chem. Phys.* 113 (2009) 334–337, <https://doi.org/10.1016/j.matchemphys.2008.07.070>.
- [36] N. Yamaguchi, R. Nakazato, K. Matsumoto, M. Kakesu, N.C. Rosero-Navarro, A. Miura, K. Tadanaga, Electrocatalytic property of Zn–Al layered double hydroxides for CO₂ electrochemical reduction, *J. Asian Ceram. Soc.* 11 (2023) 406–411, <https://doi.org/10.1080/21870764.2023.2236441>.
- [37] X. Wu, J.W. Sun, P.F. Liu, J.Y. Zhao, Y. Liu, L. Guo, S. Dai, H.G. Yang, H. Zhao, Molecularly Dispersed Cobalt Phthalocyanine Mediates Selective and Durable CO₂ Reduction in a Membrane Flow Cell, *Adv. Funct. Mater.* 32 (2021) 2107301, <https://doi.org/10.1002/ADFM.202107301>.
- [38] A.V. Ghule, B. Lo, S.H. Tzing, K. Ghule, H. Chang, Y.C. Ling, Simultaneous thermogravimetric analysis and in situ thermo-Raman spectroscopic investigation of thermal decomposition of zinc acetate dihydrate forming zinc oxide nanoparticles, *Chem. Phys. Lett.* 381 (2003) 262–270, <https://doi.org/10.1016/J.CPLETT.2003.09.125>.
- [39] M.Sreekanth Sunaina, S. Ghosh, S.K. Mehta, A.K. Ganguli, M. Jha, Investigation of the growth mechanism of the formation of ZnO nanorods by thermal decomposition of zinc acetate and their field emission properties, *CrystEngComm* 19 (2017) 2264–2270, <https://doi.org/10.1039/C7CE00073A>.
- [40] M. Alqubati, S.O.M. Osman, M.S.A. Gallil, M.A. Algrade, A. Mohammed Sultan, A. M. Qaid, Nonlinear effects of the biosynthesis temperature of ZnO nanoparticles on their structural, optical, and ultraviolet blocking parameters, *J. Opt.* (2023), <https://doi.org/10.1007/s12596-023-01394-5>.
- [41] N. Tu, H. Van Bui, D.Q. Trung, A.T. Duong, D.M. Thuy, D.H. Nguyen, K.T. Nguyen, P.T. Huy, Surface oxygen vacancies of ZnO: A facile fabrication method and their contribution to the photoluminescence, *J. Alloys Compd.* 791 (2019) 722–729, <https://doi.org/10.1016/j.jallcom.2019.03.395>.
- [42] D. Scarano, G. Spoto, S. Bordiga, A. Zecchina, C. Lamberti, Lateral interactions in CO adlayers on prismatic ZnO faces: a FTIR and HRTEM study, *Surf. Sci. Lett.* 276 (1992) A11–A12, [https://doi.org/10.1016/0167-2584\(92\)90093-k](https://doi.org/10.1016/0167-2584(92)90093-k).
- [43] G. Hitkari, S. Singh, G. Pandey, Structural, optical and photocatalytic study of ZnO and ZnO–ZnS synthesized by chemical method, *Nano-Structures & Nano-Objects* 12 (2017) 1–9, <https://doi.org/10.1016/J.NANOSO.2017.08.007>.
- [44] R.A. Mereu, A. Mesaros, T. Petrisor, M. Gabor, M. Popa, L. Ciontea, T. Petrisor, Synthesis, characterization and thermal decomposition study of zinc propionate as a precursor for ZnO nano-powders and thin films, *J. Anal. Appl. Pyrolysis* 104 (2013) 653–659, <https://doi.org/10.1016/J.JAAP.2013.05.001>.
- [45] R.A. El-Nagar, A.A. Ghanem, R.A. El-Nagar, A.A. Ghanem, Syngas Production, Properties, and Its Importance, (2019). <https://doi.org/10.5772/INTECHO.PEN.89379>.
- [46] M. Ma, B.J. Trześniwski, J. Xie, W.A. Smith, Selective and Efficient Reduction of Carbon Dioxide to Carbon Monoxide on Oxide-Derived Nanostructured Silver Electrocatalysts, *Angew. Chemie Int. Ed.* 55 (2016) 9748–9752, <https://doi.org/10.1002/ANIE.201604654>.
- [47] H. Mistry, Y.W. Choi, A. Bagger, F. Scholten, C.S. Bonifacio, I. Sinev, N.J. Divins, I. Zegkinoglou, H.S. Jeon, K. Kisslinger, E.A. Stach, J.C. Yang, J. Rossmel, B. Roldan Cuenya, Enhanced Carbon Dioxide Electroreduction to Carbon Monoxide over Defect-Rich Plasma-Activated Silver Catalysts, *Angew. Chemie Int. Ed.* 56 (2017) 11394–11398, <https://doi.org/10.1002/ANIE.201704613>.
- [48] W. Zhu, R. Michalsky, Ö. Metin, H. Lv, S. Guo, C.J. Wright, X. Sun, A.A. Peterson, S. Sun, Monodisperse Au nanoparticles for selective electrocatalytic reduction of CO₂ to CO, *J. Am. Chem. Soc.* 135 (2013) 16833–16836, <https://doi.org/10.1021/ja409445p>.
- [49] D.R. Yang, L. Liu, Q. Zhang, Y. Shi, Y. Zhou, C. Liu, F. Bin Wang, X.H. Xia, Importance of Au nanostructures in CO₂ electrochemical reduction reaction, *Sci. Bull.* 65 (2020) 796–802, <https://doi.org/10.1016/J.SCIB.2020.01.015>.
- [50] Z. Cao, D. Kim, D. Hong, Y. Yu, J. Xu, S. Lin, X. Wen, E.M. Nichols, K. Jeong, J. A. Reimer, P. Yang, C.J. Chang, A Molecular Surface Functionalization Approach to Tuning Nanoparticle Electrocatalysts for Carbon Dioxide Reduction, *J. Am. Chem. Soc.* 138 (2016) 8120–8125, <https://doi.org/10.1021/JACS.6B02878>.
- [51] J.H. Koh, H.S. Jeon, M.S. Jee, E.B. Nursanto, H. Lee, Y.J. Hwang, B.K. Min, Oxygen plasma induced hierarchically structured gold electrocatalyst for selective reduction of carbon dioxide to carbon monoxide, *J. Phys. Chem. C* 119 (2015) 883–889, <https://doi.org/10.1021/JP509967M>.
- [52] K. Hara, A. Kudo, T. Sakata, High Efficiency Electrochemical Reduction of Carbon Dioxide under High Pressure on a Gas Diffusion Electrode Containing Pt Catalysts, *Journal of the Electrochemical Society* 142 (4) (1995) L57–L59, <https://doi.org/10.1149/1.2044182>.
- [53] S. Matsuda, M. Tanaka, M. Umeda, Energy conversion efficiency comparison of different aqueous and semi-aqueous CO₂ electroreduction systems, *Anal. Methods* 14 (2022) 3280–3288, <https://doi.org/10.1039/D2AY01087A>.